JACS JOURNAL OF THE AMERICAN CHEMICAL SOCIETY

pubs.acs.org/JACS

Article

Mechanistic Analysis of Solid-State Colorimetric Switching: Monoalkoxynaphthalene-Naphthalimide Donor–Acceptor Dyads

Christopher D. Wight, Qifan Xiao, Holden R. Wagner, Eduardo A. Hernandez, Vincent M. Lynch, and Brent L. Iverson*

Cite This: J. Am. Chem. Soc. 2020, 142, 17630−17643

Read Online

ACCESS | Metrics & More | Article Recommendations | Supporting Information

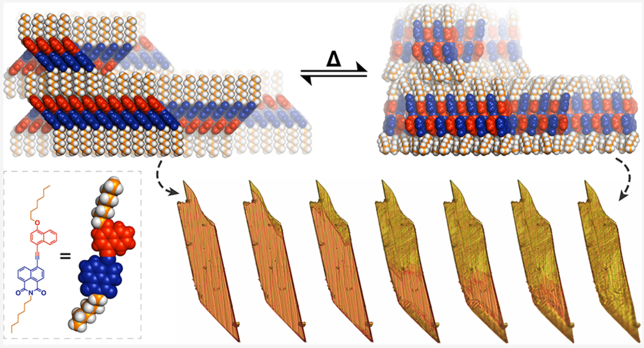

ABSTRACT: There is growing interest in creating solids that are responsive to various stimuli. Herein we report the first molecular-level mechanistic picture of the thermochromic polymorphic transition in a series of MAN-NI dyad crystals that turn from orange to yellow upon heating with minimal changes to the microscopic morphology following the transition. Detailed structural analyses revealed that the dyads assemble to create an alternating bilayer type structure, with horizontal alternating alkyl and stacked aromatic layers in both the orange and yellow forms. The observed dynamic behavior in the solid state moves as a yellow wavefront through the orange crystal. The overall process is critically dependent on a complex interplay between the layered structure of the starting crystal, the thermodynamics of the two differently colored forms, and similar densities of the two polymorphs. Upon heating, the orange form alkyl chain layers become disordered, allowing for some lateral diffusion of dyads within their own layer. Moving to either adjacent stack in the same layer allows a dyad to exchange a head-to-head stacking geometry (orange) for a head-to-tail stacking geometry (yellow). This transition is unique in that it involves a nucleation and growth mechanism that converts to a faster cooperative wavefront mechanism during the transition. The fastest moving of the wavefronts have an approximately 38° angle with respect to the long axis of the crystal, corresponding to a nonconventional C−H···O hydrogen bond network of dyad molecules in adjacent stacks that enables a transition with cooperative character to proceed within layers of orange crystals. The orange-to-yellow transition is triggered at a temperature that is very close to the temperature at which the orange and yellow forms exchange as the more stable, while being lower than the melting temperature of the original orange, or final yellow, solids.

■ INTRODUCTION

There is still a great deal to learn about the mechanisms underlying dynamic behaviors of molecules in the solid state. The higher-order structure of solids imposes severe limitations on molecular motion and dynamics. Yet, there is growing interest in creating solids that are responsive to various stimuli. An understanding of the interplay between all of the relevant noncovalent interactions is fundamental for the rational design of solids that respond with useful properties and behaviors. Electrostatic interactions of all types, including hydrogen bonding and van der Waals interactions, combine to determine the exact intermolecular geometries adopted by organic molecules and assemblies in solids, liquids, and mesophases. Over the last few decades, our understanding of the interactions between aromatic molecules has increased significantly,[1] resulting in the increased exploitation of organized aromatic molecules in numerous fields including crystal engineering,[2,3] catalyst design,[4,5] supramolecular self-assembly,[6,7] and molecular sensing.[8]

An older rationale for understanding the relative geometries adopted by interacting aromatic units, known as the "polar/π model", rationalizes aromatic stacking geometries as maximizing favorable quadrupole−quadrupole interactions between aromatic units.[9,10] Later work by Rashkin and Waters,[11] as well as computational work by Wheeler and Houk,[12,13] and more recently Wheeler,[14−17] has provided strong evidence in favor of a newer model, known as the "local, direct interaction" model[14] which postulates that the substituents on aromatic rings dictate aromatic stacking geometries as a result of local, through-space electrostatic interactions from polarized bonds. Excellent experimental work by Shimizu and co-workers

Received: July 29, 2020
Published: September 8, 2020

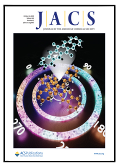

ACS Publications © 2020 American Chemical Society

https://dx.doi.org/10.1021/jacs.0c08137

utilizing molecular balances have further informed our understanding of aromatic interactions.[18−20]

The polar/π model does provide an intuitive rationale for the face-centered stacking geometry adopted by the relatively electron-rich 1,5-dialkoxylnaphthalene (DAN) and relatively electron poor 1,4,5,8-naphthalenetetracarboxylic diimide (NDI) pioneered by our group in the context of aqueous foldamers.[21−29] However, contrary to what the polar/π model would predict but consistent with the local, direct interaction model, NDI has been shown to exhibit highly favorable NDI−NDI associations in solution,[24] as well as adopt NDI offset self-stacking in a variety of contexts (Figure S1).[29−36] Previous work with alkyl-substituted DAN and NDI derivatives revealed thermochromic changes that accompany the reorganization of some DAN and NDI mixtures.[30−32] Cooling of certain DAN and NDI mixtures from the isotropic phase produced a deep red colored mesophase, with DAN-NDI adopting an alternating face-centered stacking geometry. Even more interesting, a dramatic thermochromic change occurred in some derivatives when the red mesophase cooled to form a yellow crystalline solid. Various experiments indicated this color change to be the result of the self-sorting of NDI and DAN, with offset parallel NDI self-stacking and DAN self-stacking in a herringbone geometry. Thus, NDI can be thought of as having a "split personality" in terms of its favorable stacking modes: alternating face-centered stacking with electron-rich aromatics like DAN and offset NDI self-stacking.

As part of our comprehensive supramolecular program focused on NDI and its analogs, a series of molecules were synthesized incorporating naphthalene monoimides (NI) covalently linked via an alkyne to monoalkoxynaphthalenes (MAN). Interestingly, several of these MAN-NI donor−acceptor dyads showed a dramatic difference in solid-state color between solids created from relatively faster (yellow) and slower (yellow-orange or orange) evaporation from solution.[33] In the solid-state, one of these dyads was found to change color in response to grinding (orange to yellow), heating (orange to yellow), and vapor fuming (yellow to orange), with repeatable cycles of color changing.[34] Similar to the thermochromic behavior of independent DAN and NDI mixtures previously described, the change in color was determined to result from a conformational change of the aromatic units. Upon the basis of single crystal data, X-ray diffraction (XRD) patterns, and modeling, the stimuli-responsive behavior was reported to result from a conformational switch between two stable polymorphs. When ground or heated, the orange crystalline form, possessing a head-to-head (NI−NI) stacking geometry, interconverted to a yellow soft crystalline mesophase with a head-to-tail (NI-MAN) stacking geometry that persisted at room temperature in the absence of solvent vapor, an indication that both packing geometries have kinetic stability.

Aromatic lumiphores, including the aforementioned MAN-NI dyads, are often employed in solid-state sensing. Changes in the optical properties of these materials can be achieved through synthetic modifications that alter the energy of frontier orbitals as well as changes in solid-state packing. In the solid-state, slight changes in molecular packing can dramatically alter the optical and electronic properties of conjugated materials through various mechanisms that can operate in isolation or parallel.[37−39] For example, long-range electronic coupling between molecules, that is dependent on the alignment of transition dipole moments, can alter the spectroscopic properties of solid-state systems compared to free molecules.[39] In addition, short-range intermolecular interactions that manifest through direct orbital overlap, especially through LUMO−LUMO and HOMO−HOMO overlap, can facilitate the delocalization of locally excited states into delocalized excitonic charge-transfer (CT) states.[38,39] While these intermolecular excitonic interactions are distinct, the net electronic coupling experienced is a product of the interference between short- and long-range coupling.[39]

Many materials exploit polymorphism as a functional property that allows some form of reporting.[40] Polymorphic phase transitions have been reviewed in experimental,[41] computational,[42] and theoretical contexts.[43] Stimuli induced polymorphic color switching has been achieved in the solid-state following the application of various types of external stimuli including heat,[34] pressure,[44] mechanical force,[45] and exposure to various analytes including salts[46] and solvent.[47] Covalent modifications of polymorphic systems have been effectively used to impart tunability in various thermochromic systems.[30,48] Fang and colleagues have shown that self-assembled thermochromic supramolecular systems can be formed that allow for tunability of transition temperature and colors based on competing CT interactions in both gels and the solid-state.[49−51]

Although it is the aromatic π-system that directly influences the electronic and photophysical properties of the system, substituents appended to aromatic molecules are a critical and determining factor in the solid-state electronic,[52] spectroscopic, and stimuli-responsive properties of solid-state stimuli-responsive systems.[53] An example of utilizing substituents on aromatic systems to influence photophysical properties in the solid-state came from Ito and co-workers, presenting a design principle for stimuli-responsive color switching materials that exploit polymorphism through competing interactions between aromatic lumiphores and appended side chains.[46] By constructing amphiphilic and dipolar characteristics into a single molecule, different metastable polymorphic states were stabilized through competing intermolecular interactions of the dipolar aromatic core, a hydrophilic side chain, and a hydrophobic side chain. It is worth noting that this system self-assembled through the formation of alternating aromatic, hydrophilic, and hydrophobic layers, analogous to what is reported here. The same group has also reported stimuli-responsive systems that exploit the switching between multiple accessible polymorphs through mechanically induced crystal-to-crystal transformations.[41,45,54,55]

Despite improvements in our understanding of polymorphism, targeted polymorphism still remains a highly desirable goal.[56] Computational efforts have successfully modeled polymorphic transformations but have been limited to small molecules[57−59] or larger, rigid systems.[60] Experimental insights into the mechanisms by which polymorphs interconvert would better inform the future design of novel polymorphic systems. While numerous examples for color changing materials that rely on polymorphism exist, elucidating the molecular mechanisms by which these materials interconvert is experimentally challenging because many experimental techniques employed only provide a time and space average of structural information.[42] Application of external stimuli to polymorphic systems containing flexible substituents (e.g., alky chains) often involve switching between crystalline and noncrystalline states, with structures of the latter often being inferred from structural information like powder XRD.[34,46] A subset of reports on polymorphic transitions have been able to correlate macroscopic changes to specific nanoscopic reorganization.[59,61−70] For example, Ito and co-workers correlated molecular rearrangements to macroscopic mechanical motion from the anisotropic strain release in thermosalient crystals.[70] This thermosalient effect illustrates one of the two general polymorphic transition mechanisms seen in organic crystals, involving a rapid, cooperative displacement of molecules, that is referred to by multiple names including martensitic, displacive, or cooperative transitions.[42,69] The other general polymorphism mechanism seen in organics is a nucleation and growth type mechanism that, as the name implies, operates analogous to the mechanism of crystal growth from solution[42] and is noted to often disrupt the integrity of the initial crystal.[69]

Herein we report the first molecular-level mechanistic picture of the thermochromic polymorphic transition of the MAN-NI dyads. In contrast to previously reported polymorphic systems that exploit alkyl chains,[64,68] the stimuli-induced thermochromic transition of our MAN-NI dyads proceeded without altering the microscopic morphology of the original crystal while simultaneously exhibiting a dramatic visible color change. Comprehensive standard and in situ heating XRD, grazing-incidence wide-angle X-ray scattering (GIWAXS), noncontact atomic force microscopy (AFM), polarized optical microscopy (POM), spectroscopy, and differential scanning calorimetry (DSC) analyses were used to develop a full picture of the thermochromic process. Our analysis revealed that the MAN-NI dyads appear to be the first example of a polymorphic system involving a nucleation and growth mechanism that converts to a faster cooperative mechanism during a transition. The transition critically depends upon a complex interplay between the overall layered structure of the starting crystal, the thermodynamics of the two differently colored forms, and similar densities of the interconverting polymorphs. These insights will expand applications of polymorphic switching systems, allowing for a new level of control over programmed dynamic material properties without morphological changes.

■ MATERIALS AND METHODS

Synthesis of all dyads followed known procedures.[33] Experimental procedures and methods, crystallization conditions, synthetic protocols, and characterization of all dyads and intermediates can be found in the Supporting Information.

■ RESULTS

Stimuli-Responsive Behavior. Consistent with our previous reports,[33,34] most of the dyads in this study (Figure 1) could crystallize as orange (**O**) or yellow (**Y**) polymorphs (Figure S2) depending on crystallization conditions (specific crystallization conditions are detailed in Scheme S2).

When orange crystals of **6**, **7**, and **8**, referred to here as **6O**, **7O**, and **8O**, respectively, are heated beyond 100 °C, the orange crystals transition to a soft-crystalline yellow material that persists indefinitely upon cooling. Reversal back to the orange crystalline phase occurs in less than 24 h when exposed to DCM vapor in a fuming chamber.[34]

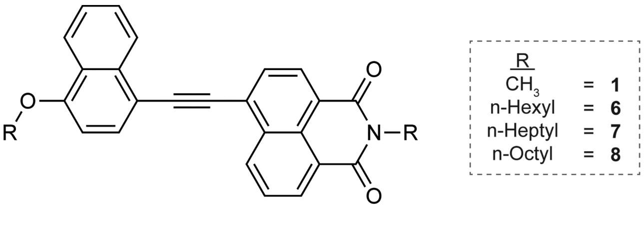

Figure 1. Structure of the MAN-NI dyads used in this study.

Uniquely, **1** was the only derivative studied that could only be grown as a single polymorph and crystallized as bright orange needles (**BO**). When heated, **1BO** crystals do not form a yellow material and sublime at 284 °C (Figure S3).

Color Switching Moves Most Quickly as a Wavefront Through the Crystal. When orange crystals of **6**, **7**, and **8** are heated, they transform to a yellow material (designated as **Y*** in the following discussion) prior to melting. Examination of this thermochromic orange-to-yellow conversion under a POM equipped with a heating stage revealed that thermally generated yellow material retains the overall microscopic morphology of the starting orange crystal (Figure 2, Movie S1, and Movie S2).

Remarkably, numerous heating experiments of orange crystals under a POM verified that the thermochromic transition proceeds as one or more wavefronts moving through the orange crystal. It is assumed that a structural transition is occurring at the orange-yellow wavefront interface. The transition generally is observed to start at a crystal edge or a small crack/defect in the crystals. The fastest moving orange-to-yellow wavefronts proceed parallel to the long axis of the crystal, as shown in Figure 2. The widest and fastest moving of these wavefronts move at speeds on the order of 12 μm s^{-1} and are generally diagonal in nature, exhibiting an average angle of 38 ± 4° relative to the long edge of the crystal (Figure 2c). When viewed from above the crystal, horizontal wavefronts move parallel to either crystal edge and proceed slower through the crystal, with speeds on the order of 0.2−0.5 μm s^{-1}. Importantly, the slower horizontal waves have been observed to "turn", and as the angle becomes more pronounced, the wavefront speed also increases (bottom of crystal in Figure 2c, Movie S2). As the wavefront passes, the surface features and overall dimensions of the material only change slightly. For the **6O** crystal shown in Figure 2c, after heating from orange to yellow the average dimensions of the crystal grew 2.038 μm (0.21%) in length, 2.049 μm (1.1%) in width, and 0.213 μm (2.8%) in height, all while maintaining similar microscopic features.

In thicker crystals, multiple wavefronts were generally seen, apparently caused by multiple wavefronts moving through different horizontal layers within the crystal. Thicker crystals exhibited more of these waves. Thinner crystals appear to have only one or a few transition layers. Thicker crystals were also noted to deform or bend less during the thermal transition as compared to thinner crystals, like the **7O** crystal shown in Figure 2a that begins to bend upward in the second-half of the transition.

Spectroscopic Characterization. In solution, all dyads had nearly identical spectroscopic properties, as the alkyl side chains do not affect electronic properties within the aromatic core. Dyads were shown to exhibit significant solvatochromism (Figure 3), with a strong bathochromic shift with solvents of increasing polarity (hexanes $\lambda_{\text{em-max}}$ = 444 nm, acetonitrile, $\lambda_{\text{em-max}}$ = 593 nm, Figure 4). This shift is consistent with a highly charge-separated excited state due to electron transfer from the electron-rich MAN core to the electron-deficient NI core. This is further supported by **7** having a calculated excited state dipole of 14.64 D in the first electronically excited state, compared to just 7.21 D in the ground state (ωB97X-D, 6-

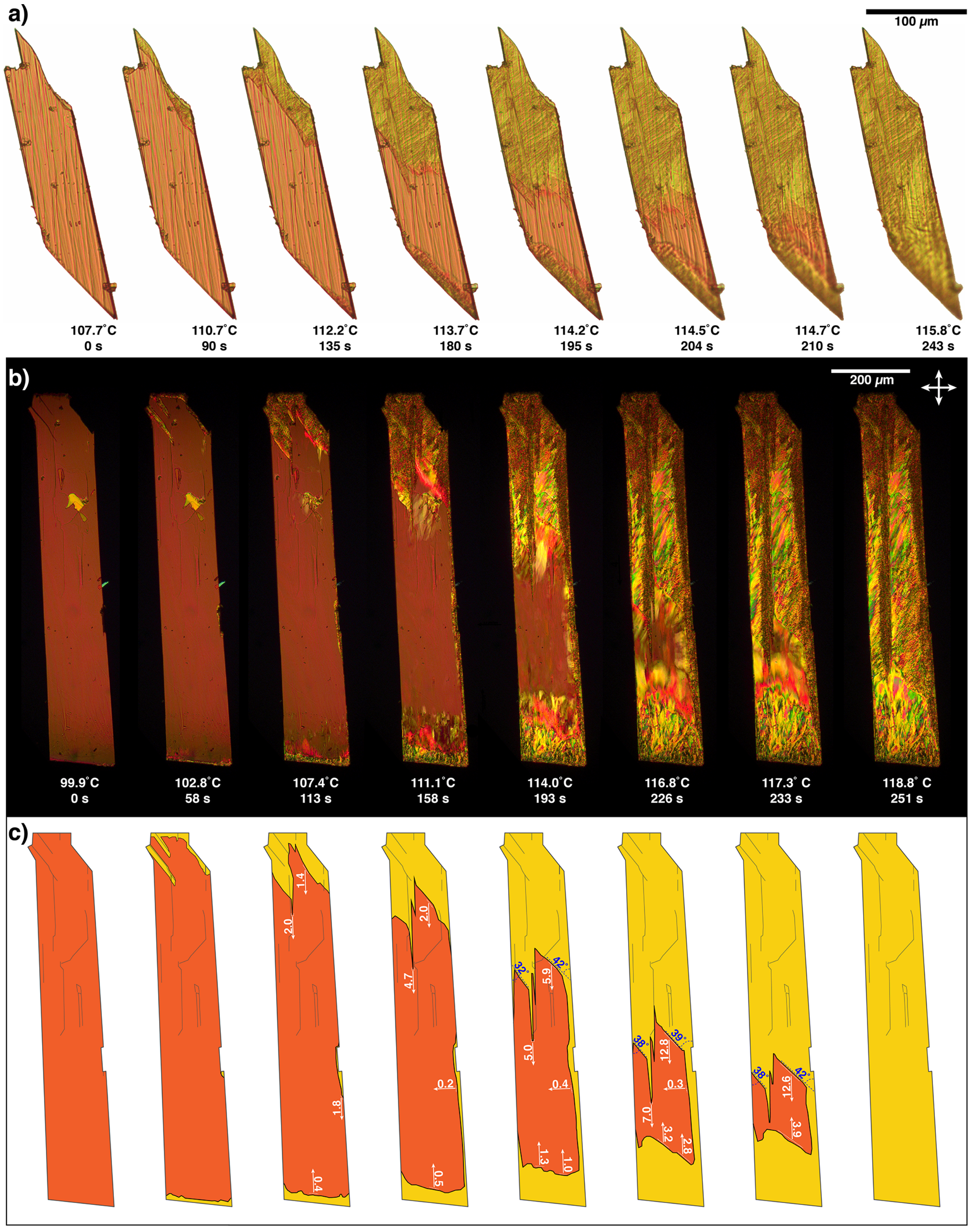

Figure 2. Visualized under a microscope equipped with a heating stage, orange crystals are thermally converted to a yellow material that persists indefinitely after cooling. Time and temperature for each image are provided below each crystal. (a) A single **7O** orange crystal is heated at 2 °C min^{-1} to form **7Y***. (b) A single **6O** crystal is heated under a cross polarized microscope at 5 °C min^{-1} to form **6Y***. (c) Cartoon depiction of thermally induced changes occurring during the **6O** to **6Y*** transition in the corresponding images above, with yellow coloring denoting complete transition to the yellow form through all layers of the crystal. Inside the cartoon in white, arrows show the direction of the wavefront movement and adjacent values representing the speed of the wavefront in μm sec^{-1}. The angle of the wavefront relative to the indicated long axis of the crystal is shown in blue.

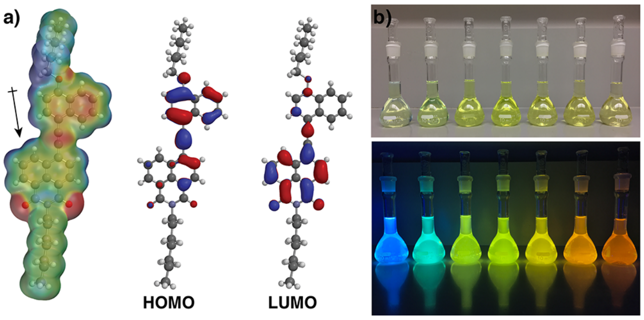

Figure 3. (a) Calculated dyad electrostatic potential, molecular dipole, HOMO, and LUMO of 7 (ωB97X-D, 6-311+G**). (b) 7 in solvents of increasing polarity from left to right: hexanes, toluene, ethyl acetate, THF, DCM, acetone, and MeCN. Bottom: UV irradiated samples, showing positive solvatochromism.

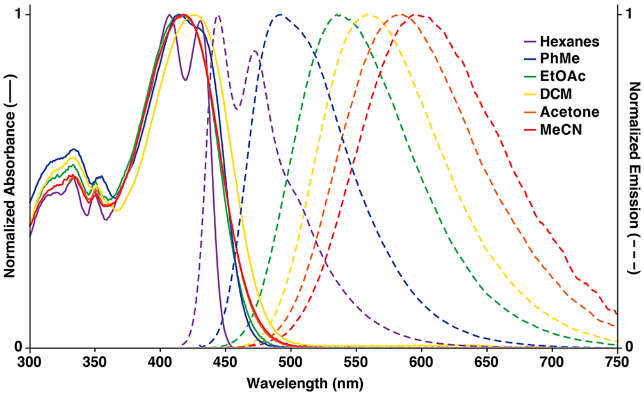

Figure 4. Normalized absorbance and emission spectra for 7 in a variety of solvents.

311+G**). A summary of dyad spectroscopic properties in solution, including quantum yields and fluorescence lifetimes, can be found in Table S1 and Figure S4.

For **6**, **7**, and **8** in the solid-state, orange and yellow crystals had very similar absorbance and emission profiles. Orange crystals had red-shifted absorbance and emission profiles relative to their yellow counterparts (Figure 5). Note that the exact emission maxima of orange crystals showed variability that appears correlated to crystal size, with some observed red-shifting as crystal size increases (Table 1).

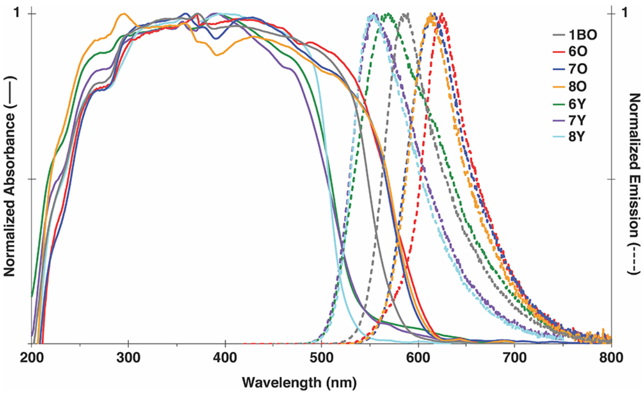

Figure 5. Solid-state absorbance and emission for dyad derivatives grown as crystals.

Table 1. Solid-State Absorbance and Emission for Dyad Derivatives

compound	$\lambda_{\text{abs-max}}$ (nm)	$\lambda_{\text{em-max}}$ (nm)
1BO	371	590
6O	371	625
7O	360	617
8O	296	613
6Y	392	569
7Y	390	554
8Y	395	554
6Y*	393	561
7Y*	392	566
8Y*	392	563

For yellow crystals, **7Y** and **8Y** showed nearly identical absorbance and emission spectra (Table 1). In comparison, the emission of **6Y** has a small bathochromic shift relative to **7Y** and **8Y**.

A comparison of solid-state spectroscopic properties between the **O**, **Y**, and **Y*** forms for each **6** and **7**, and **8** is shown in Figure 6 and Figure S5, respectively. In general, **Y** and **Y*** have closely matching absorption and emission spectra for all three of these derivatives. For **7** and **8**, **Y*** emission profiles have a small bathochromic shift compared to their **Y** counterparts, while **6Y*** shows a small hypsochromic shift in comparison to **6Y** (Figure 6).

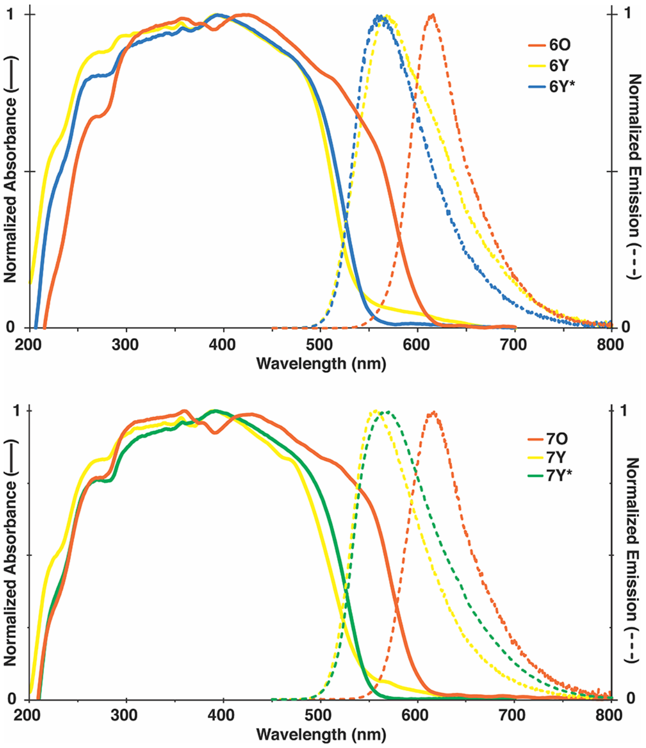

Figure 6. Solid-state absorbance and emission comparing grown yellow (**Y**) to thermally produced yellow (**Y***) derivatives of **6** (top) and **7** (bottom).

DSC Thermal Transition Characterization. DSC was used to further characterize the orange-to-yellow transition for **6**, **7**, and **8**. The DSC traces of each derivative shows two endothermic peaks corresponding to the **O** to **Y*** phase transition and the subsequent melting of **Y*** to the isotropic phase (Figure 7). Cooling from the isotropic phase generates the yellow material that is similar to **Y*** as shown by successive heating-and-cooling cycles (Figure S6). Once heated to **Y***, this form persists indefinitely for each derivative, even when cooled extremely slowly. For example, when **7O** was heated to produce **7Y***, the **7Y*** form persisted even when cooled at the slowest obtainable rate of 0.1 °C min^{-1} (Figure S7).

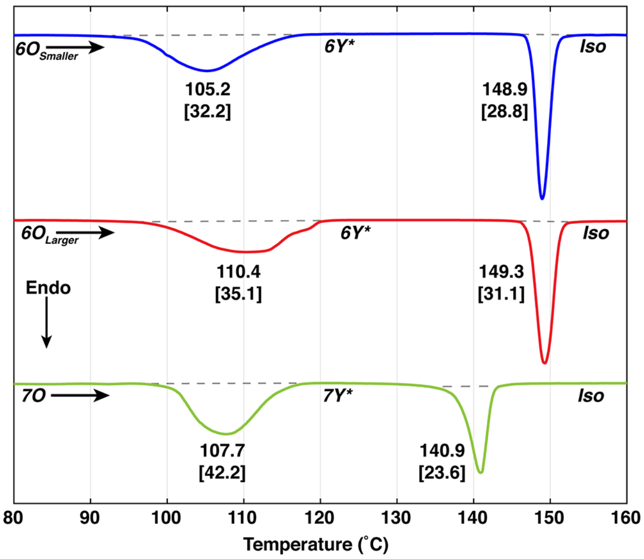

Figure 7. Heated at 5 °C min^{-1}, DSC curves show orange crystals (**O**) being thermally converted to a yellow material (**Y***) prior to melting to the isotropic phase (Iso). Values near peaks show the corresponding peak temperature (°C), bracketed values represent integrated transition enthalpy (kJ mol^{-1}). Larger **6O** crystals are seen to transition from orange-to-yellow at higher temperatures and require more energy.

Orange-to-yellow and yellow-to-melt transition temperatures and enthalpies for the dyads **6**, **7**, and **8** are presented in Table S2. In general, when the respective orange crystals of similar size are heated for the different derivatives, the longer the side chains, the larger the enthalpy of transition for the **O** to **Y*** conversion. In addition, similarly sized yellow crystals grown from derivatives with longer side chains melt to the isotropic phase with increasing enthalpies of transition ranging from 24.10 to 34.69 kJ mol^{-1} for **6Y-8Y**, respectively (Table S2). Importantly, compared to the grown yellow crystals (**Y**), thermally generated **Y*** in general melts to the isotopic phase with less energy as shown by comparatively lower transition enthalpies. However, care must be taken when interpreting the differences between derivatives, as we observed that crystal size influences the transition temperature and transition enthalpies measured for both the **O** to **Y** transition and the **Y*** to the isotropic phase transition. For example, as shown in Figure 7, larger **6O** crystals ($\mathbf{6O}_{\text{Larger}}$) transformed to **Y*** at higher temperatures, with larger enthalpies of transition, compared to smaller **6O** crystals ($\mathbf{6O}_{\text{smaller}}$). Melting of **6Y*** to the isotropic phase followed the same size-dependent trend.

Atomic Force Microscopy (AFM). Morphological changes accompanying the thermal conversion of **O** to **Y*** were investigated using AFM. Noncontact AFM of a single **7O** orange crystal reveals clean, sharp edges (Figure 8). Thermal conversion of this single crystal to **7Y*** and subsequent imaging shows the general crystalline shape is maintained following conversion, while the surface has nanoscopic feature changes including the formation of numerous ridges/steps.

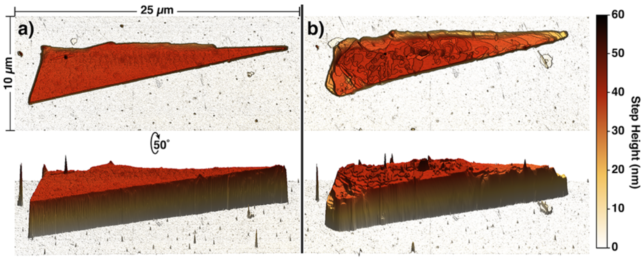

Figure 8. Noncontact AFM generated 3D profiles of the same crystal before and after heating, showing retention of overall shape with nanoscopic surface changes. (a) Image of **7O** crystal before heating. (b) Image of the same crystal following thermal conversion to **7Y***.

Noncontact AFM measurements of **7O** microcrystals indicated the presence of lamellar structures present with a step height of ∼1.3 nm (Figure 9), roughly the height of the aromatic core in the dyad molecule. The general dimensions and lamellar structure are maintained following heating; however, nanoscopic changes to the shape of individual layers were observed (Figure 9). The differences in layer shapes after heating are interpreted to indicate that the layers underwent

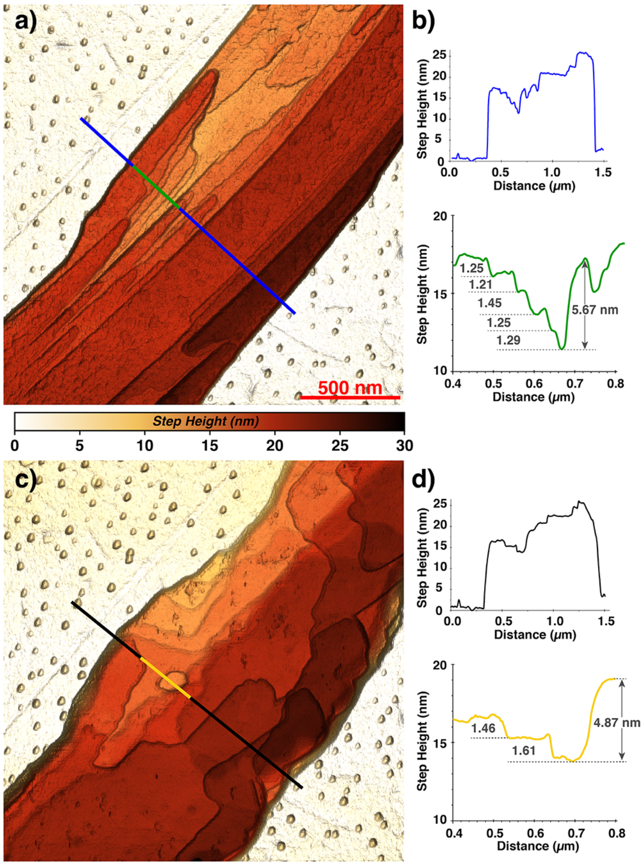

Figure 9. Noncontact 3D AFM image of single **7** crystal before and after heating showing nanoscopic surface changes following heating. (a) 3D image of a single **7O** crystal. (b) Step-height profile of the blue trace (top) and the inset green trace (bottom) in the adjacent **7O** AFM image. (c) 3D image of the same region as panel (a) after conversion to **7Y***. (d) Step-height profile of the black trace (top) and the inset yellow trace (bottom) in the adjacent **7Y*** AFM image.

structural transitions somewhat independently from each other.

Structural Characterization. In addition to the single-crystal structure of **8O** previously reported,[34] eight unique crystal structures were solved for the four dyads in this study by single-crystal X-ray diffraction. A summary of the crystallographic data for all dyad crystal structures is present in Table S3.

Different crystallization methods were employed to grow either the orange or yellow crystals as detailed in the Scheme S2. In general, for a given dyad, orange crystals grew shorter and wider compared to their longer, more needle-like yellow counterparts (Figure S2). Orange polymorphs formed in solution were better diffracting, higher quality crystals with smaller R-factors and no atoms with multiple site occupancies. Yellow polymorphs had more disorder, especially in alkyl side chains.

Orange is Head-to-Head, Yellow is Head-to-Tail. For the derivatives **6**, **7**, and **8**, multiple polymorphs were found. For these three molecules, two general packing motifs were consistently observed: orange crystals (**O**) were always observed to be stacked with the dyad cores in a head-to-head geometry[34] and yellow crystals (**Y**) were always observed to be stacked with the dyad cores in a head-to-tail geometry (Figure 10). Two structures were solved for yellow hexyl (**6Y** and **6Y′**) and heptyl (**7Y** and **7Y′**) polymorphs, with each set of polymorphs having similar packing of aromatic cores and the largest differences being manifest in side-chain packing. Uniquely, and despite examining dozens of growth conditions, **1** only crystallized as a single polymorph (**1BO**), forming bright orange needles (Figure S2). Detailed crystal packing figures for **O**, **Y**, and **1BO** crystals are shown in Figures S9, S10, and S11, respectively. It is important to note, all of the solved crystal structures only contain the pure dyad; solvent was never observed within the crystalline lattice.

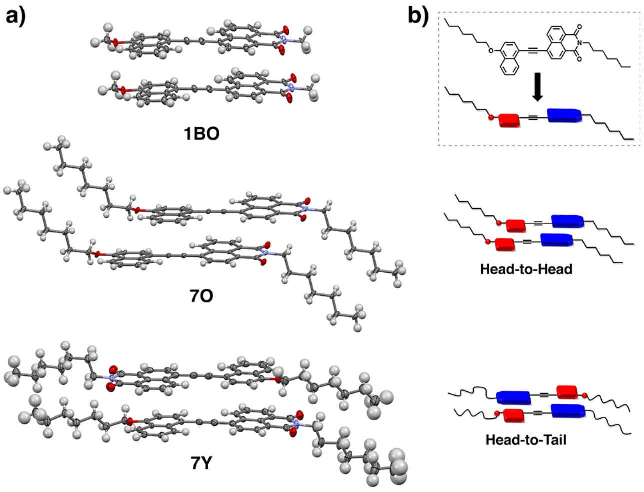

Figure 10. Single-crystal X-ray diffraction structures and cartoon depiction of dyad polymorph packing. (a) Crystal structure of **1BO**, and representative orange (**7O**) and yellow (**7Y**) crystal structures shown as displacement ellipsoids set to the 50% probability level. (b) Cartoon representation of dyad head-to-head and head-to-tail packing geometry.

Crystal Packing. In all crystals, the dyads pack to form 1-dimensional columns formed from stacking of the aromatic dyad cores. The spacing between aromatic cores is similar in all crystals, with an average distance of 3.38 ± 0.02 Å. The relative position of an adjacent dyad within the same column can be described by a molecular slip about the long and short axes of the dyad (inset, Figure 11a). As shown in Figure 11a, the **O** and **Y** polymorphs have distinctly different slip-stacking geometries, with clustering among all of the **O** and **Y** polymorphs, respectively.

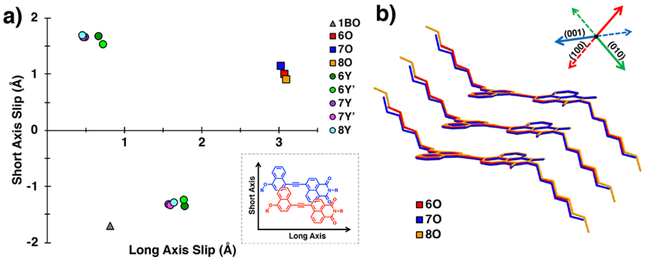

Figure 11. (a) Calculated dyad slip for **O** (squares), **BO** (triangle), and **Y** (circles) dyad polymorphs. Inset: adjacent dyads within a column are offset with displacement along the long and short axis of the dyad. (b) Overlay of **6O**, **7O**, and **8O** single-crystal structures shows the similarity in packing for all **O** crystals. Hydrogen atoms omitted for clarity and crystallographic axes inset.

All three **O** polymorphs have very similar slip-stacking, with a long axis displacement of 3.07 ± 0.03 Å and a short axis displacement of 1.0 ± 0.1 Å as illustrated by the overlay of crystal structure trimers of **6O**, **7O**, and **8O** in Figure 11b. In head-to-tail **Y** polymorphs, slip-stacking can be calculated relative to either one of the two molecules in the asymmetric unit, and hence, two values can be calculated that describe the slip-stacking geometry for the **Y** polymorphs. In both cases, there is similar slip-stacking within all **Y** polymorphs. While **1BO** stacks in a head-to-head geometry, it has a unique slip-stacking geometry with its largest offset along the short axis of the dyad, in contrast to the head-to-head stacked **O** dyads (**6O**, **7O**, and **8O**).

In the three **O** polymorph crystals, aromatic cores in adjacent columns are nearly perpendicular about the long axis of the dyad, with an average intercolumnar angle of 87.4 ± 0.4° (Figure S9). In contrast, aromatic cores in adjacent columns of **Y** crystals are either parallel (**6Y** and **6Y′**) or rotated about the short axis of the dyad between 48−49° (**7Y**, **7Y′**, **8Y**) (Figure S10).

The overall packing of molecules within the representative crystal structures is shown in Figure 12. For both the orange and yellow polymorphs, the long axis of the crystals correspond to what is most likely to be the strongest intermolecular interactions, the electrostatic attractions between aromatic dyad cores. The short axis of the crystal is formed from alternating aromatic and aliphatic layers.

Aliphatic Layer Packing Differences. In all polymorphs, the dyads assemble to create an alternating bilayer type structure, with alternating alkyl and aromatic layers (Figure 12). However, the nature of alkyl chain packing differs markedly between the **O** and **Y** polymorphs. Crystal structures of all **O** polymorphs have alkyl chains in staggered-anti conformations, with side chains from adjacent layers interdigitating, forming a close-packed zipper-like structure (Figure 12d). Alkyl side chains in **Y** crystals show more disorder and adopt mixtures of staggered-anti and gauche conformations and have segregated (i.e., not interdigitated) side chains (Figure 12f). Disorder in **Y** side chains is seen with

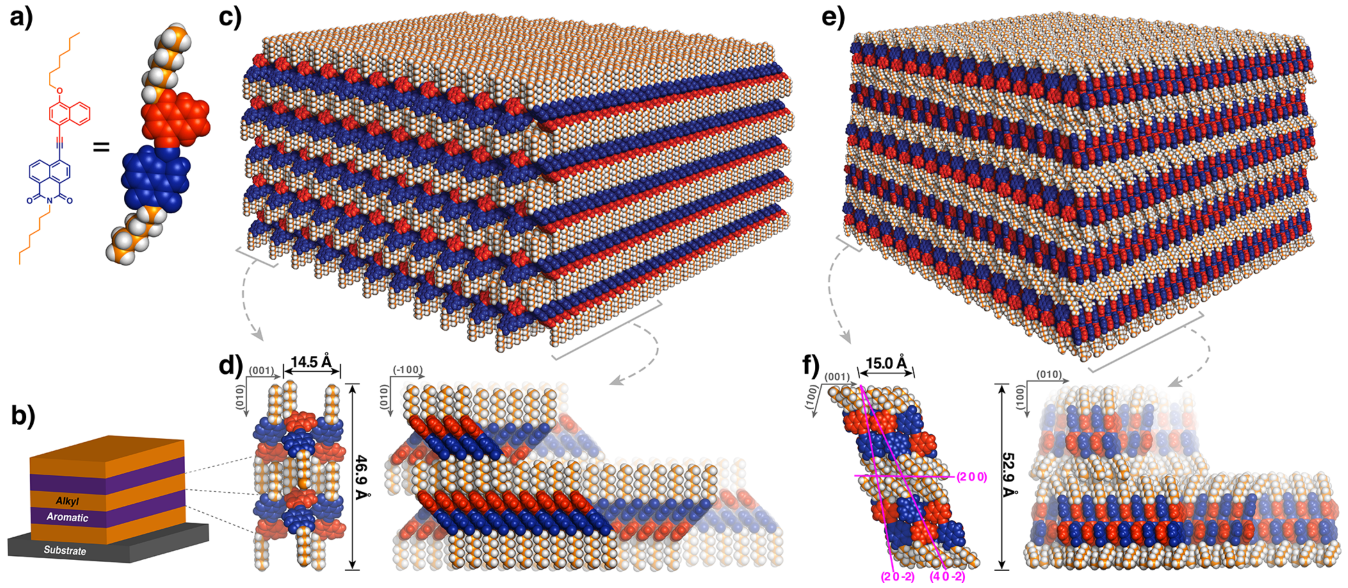

Figure 12. (a) Representation of 7 as shown in bilayer packing schematics. (b) Cartoon illustrating preferred orientation for both **O** and **Y** polymorphs, where alternating alkyl and aromatic layers are parallel to the substrate. (c) Schematic of **7O** packing. (d) Crystal structure of **7O** showing head-to-head dyad core stacking geometry, perpendicular columns relative to the long axis of the dyad molecule, and interdigitated side chains. (e) Schematic of **7Y** packing. (f) Crystal structure of **7Y** showing head-to-tail dyad core stacking geometry, adjacent columns tilted 49° relative to the short axis of the dyad molecule, and segregated side chains. Select crystallographic planes of **7Y** are shown in magenta.

larger thermal displacement ellipsoids associated with side chains of **Y** crystals and multiple site occupancies for one side chain in the asymmetric unit of **6Y**, **7Y**, and **7Y′** (Figure S10, Table S3).

Importantly, in **O** crystals, the orientation of the dyads of adjacent columns alternate as shown in Figure 12d. In other words, if a given aromatic stack in an **O** crystal has the MAN units of the dyads oriented "upwards" in the crystal, both adjacent columns within the same layer will have the NI units oriented "upwards", and *vice versa*.

The nearly perpendicular relationship between columns in all **O** crystals appear to be stabilized through a combination of favorable side chain packing and electrostatic interactions between the most polarized bonds in the dyads, namely the imide carbonyl C−O bonds and the C−H bonds of alkoxy O−CH_2 groups of the MAN units as shown by dashed green lines in Figure 13a. These proposed C−H···O hydrogen bonds create a zigzag network of connected dyads in the same layer of the crystal, and as seen in Figure 13, the molecules linked in this way trace out an angle between 37−38°, relative to the long axis of the aromatic stacks, in **6O**, **7O**, and **8O**.

Crystal Size Changes. The calculated density of **7O** and both **7Y** polymorphs, as determined from single-crystal structures, are 1.25 and 1.22 g cm^{-3}, respectively. On the basis of the differences in density of **7O** and either **7Y** polymorph, a single-crystal-to-single-crystal transition from the more dense **7O** to the less dense **7Y** would theoretically cause an increase in volume of ~2.5%. Optical profilometer measurements of individual **O** crystals before and after heating to **Y*** were used to quantify volume changes after the transition. Crystals of **7O** adsorbed onto a silicon substrate showed a 4.4 ± 0.5% increase in crystal volume after heating **7O** crystals to **7Y*** (Table S4), similar to that expected based on **7Y** crystal structures.

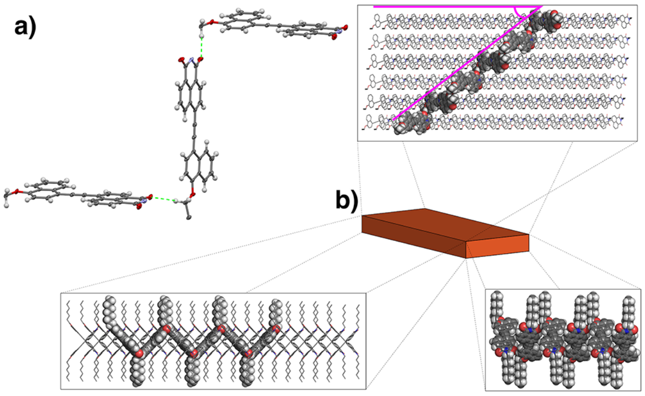

Figure 13. (a) Single-crystal structure of **7O** illustrating intermolecular C−H···O hydrogen bonds (dashed green lines) between adjacent columns. Terminal side chain atoms removed for clarity. (b) Cartoon depiction of typical orange crystal dimensions with preferred orientation: crystal long-axis is made from dyads stacked in columns, while the height of the crystal is made from alternating aromatic and alkyl layers. Projecting out of the cartoon is the **7O** crystal structure as viewed from each unique crystal face, with H atoms omitted on the line structures for clarity. Shown in space-filling mode, six dyad molecules connected through the intercolumnar C−H···O hydrogen bonding in panel (a). (Top Right) In magenta: when viewed from above the crystal, this intermolecular H-bonding network creates an angle relative to the long axis of the crystal of 37.5° in **7O** (shown in magenta) and 37.2° in **6O**.

Thin Films. Dyad 7 was deposited onto quartz substrates using physical vapor deposition and produced a yellow thin film. Vapor annealing with DCM in a fuming chamber afforded a thin film of **7O** as discrete microcrystals that were characterized by structural and spectroscopic measurements (Figure S12). GIWAXS of **7O** thin films (Figure 14) corroborated sample crystallinity and preferred orientation seen in AFM measurements (Figure 9).

Molecular Orientation in the Crystals. The **7O** polycrystalline films were characterized by a dominant orientation preference for the (010) crystallographic axis to be normal to the quartz substrates[71] (Figure 12d, 14a). The

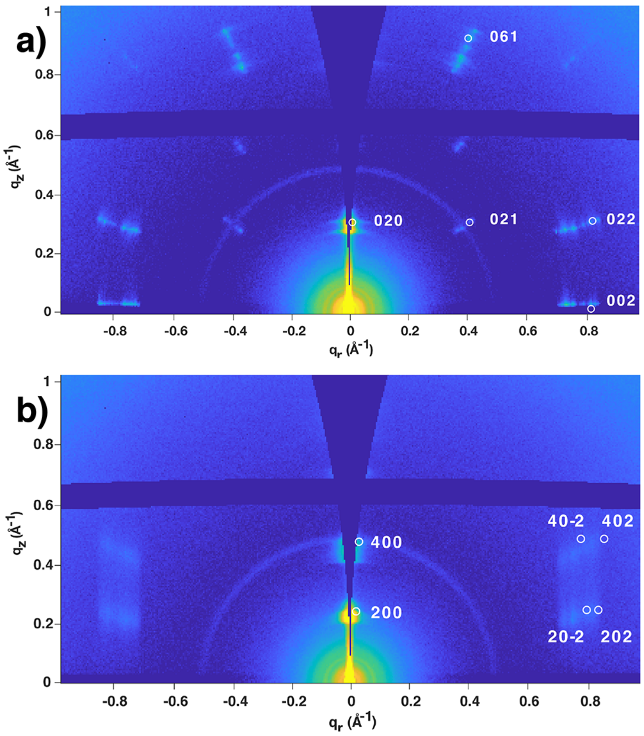

Figure 14. GIWAXS scattering pattern for thin films of **7** on a quartz substrate before and after heating. (a) Scattering pattern for **7O** polycrystalline thin film. (b) Scattering pattern for **7Y*** thin film produced from heating the **7O** thin film shown in panel (a). Inside each diffraction pattern, white circles show the calculated diffraction spots (transmission) and corresponding Miller indices based on lattice parameters from single-crystal structure data for (a) **7O** and (b) **7Y**, with preferred orientation with the crystallographic long axis perpendicular to the substrate.

combination of GIWAXS scattering data and noncontact AFM indicate the dyad formed a bilayer type lamellar structure with alternating alkyl and aromatic layers (Figure 12b, c, and e).

In agreement with the thermochromic conversion of a single crystal of **7O** to **7Y***, heating of a **7O** polycrystalline thin film generated the corresponding **7Y*** thin film as confirmed by spectroscopic (Figure S12) and GIWAXS measurements (Figure 14b). GIWAXS of the **7Y*** thin film reveals that the structure of **7Y*** is not crystalline following thermal conversion but is best described as a liquid-crystalline mesophase. Figure 14b shows scattering of the **7Y*** thin film with in-plane diffractions that correspond to the (200) crystallographic axis perpendicular to the substrate. The other diffuse diffraction spots seen in the **7Y*** scattering data match the expected location calculated[72] for the (20−2) and (40−2) crystallographic planes of **7Y**. As shown in Figure 12f, the (20−2) and (40−2) planes pass through columns of the aromatic cores and observed scattering in these locations is interpreted to represent periodic order within columns. Taken together, these structural data reveal that the **7Y*** thin film has the same lamellar structure as **7O** and that there is periodic order within columns of dyads. An increase in amorphous scattering at larger scattering angles in **7Y*** thin films indicates that some disorder is present. In-plane scattering from **7Y*** thin filmsin the (*h*00) plane occurs at a smaller scattering angle than would occur for **7Y**, based on calculated diffraction spots from **7Y** crystal structure lattice parameters. This smaller observed scattering angle of the (*h*00) planes in the **7Y*** thin film is indicative of a slightly larger (~3 Å) lamellar spacing in **7Y*** compared to **7Y**.

Structural Changes During Polymorphic Transitions in Polycrystalline Samples. In an effort to elucidate the structural changes that accompany the transition from **O** to **Y**, in situ heating XRD experiments were conducted. Numerous **6O** and **7O** crystals were placed on a heating stage inside of a diffractometer and heated, while short transmission X-ray exposures (e.g., 30 s) were taken during heating. The cross section of the X-ray beam is much larger than all transition wavefronts seen under a POM, meaning that these exposures are more of a bulk measurement that includes the **O** to **Y*** transition wavefront, as well as regions of growing **Y*** and shrinking **O**. Despite these challenges, these measurements revealed that the transition from **O** to **Y*** proceed through an amorphous transition state. As **7O** is heated, the few spots that satisfy the Bragg condition are seen to weaken in intensity before disappearing. Quickly following this gradual disappearance of **7O** diffraction spots, diffraction spots from **7Y*** appear in rapid succession, with scattering from **7Y*** lamellar spacing being observed before scattering from dyad stacks is observed (Movie S3, Figure S13).

■ DISCUSSION

Polymorph Color Differences. Absorbance of visible light by dyad molecules results in the intramolecular electron transfer from the HOMO, centered largely on the electron-rich MAN unit (see Figure 3) to the LUMO, centered largely on the electron deficient NI unit. This electron transfer is responsible for the striking solvatochromic behavior of the dyads in solvents of different polarities and is expected for such highly polarized excited states.

The key structural difference in solid-state between **O** and **Y** polymorphs is the orientation of adjacent dyad molecules within a given aromatic stack. Adjacent dyads in **O** polymorphs have offset head-to-head stacking geometries, while **Y** polymorphs exhibit head-to-tail stacking geometries. In other words, in the dyad stacks of **O** polymorphs, a given MAN unit is situated above and below MAN units of adjacent dyads, and NI units are adjacent to NI units on adjacent molecules. In this head-to-head packing arrangement, there is a small short-axis offset and a larger ~3 Å offset along the long axis of the molecule, where dyads shift unidirectionally in a column, much like the offset of stairs in a staircase (Figure 11, S9). The offset head-to-head stacking geometry in the **O** form will lead to mixing of LUMO orbitals since orbital lobes of similar phase are in close proximity (Figure S14). This LUMO mixing can facilitate the dissociation of an initial locally excited state into charge-transfer states, where electrons and holes are delocalized onto multiple molecules. This is believed to be the basis for the red-shift seen in all **O** crystals. At the quantitative level, differences in the precise geometry of LUMO orbital overlap due to slightly different displacements along the short and long molecular axes can be used to explain subtle differences between the optical properties of **O** polymorphs.

While dipolar coupling may be in play, it is not expected to be the basis for the red-shift seen with orange crystals. A comparison of the crystal structure of **1BO** to all **O** polymorphs (Figure S11, S9, respectively) shows that **1BO** also has dyads stacked in a head-to-head fashion; however, they are offset along the short molecular axis (Figure 11a). Compared to all **O** polymorphs, the smaller red-shift in **1BO** is attributed to a decrease in short-range coupling derived from orbital overlap. The small observed red-shift in **1BO** compared to all head-to-tail **Y** polymorphs is believed to result from dipolar coupling within head-to-head stacked **1BO** crystals, while the short axis offset is believed to prevent the favorable orbital overlap that resulted in the larger red-shift observed in **O** polymorphs. All **Y** polymorphs exhibit head-to-tail stacking geometries and show greater variation in slip-stacking geometry compared to the **O** polymorphs (Figure 11a). The absence of a red shift in **Y** polymorphs is interpreted to indicate that MAN-NI dyads do not form CT complexes in head-to-tail packing geometries, possibly due to energetic differences that minimize HOMO−LUMO orbital mixing.

Orientations of Dyad Molecules in the Crystals. Through a combination of transmission and GIWAXS experiments, done on both single and polycrystalline samples, as well as prediction of crystal morphology using Bravais, Friedel, Donnay, and Harker (BFDH) calculations from single-crystal data, the orientation of the dyad molecule long axis in each polymorph was determined (Figures 12 and 13). The orange materials (**6O**, **7O**, and **8O**) are structurally analogous to a nice lasagna, with the relatively thick "noodle" layers comprised of highly ordered, close-packed alkyl chains entirely in the staggered-anti conformation, interdigitated with alkyl chains from both adjacent layers. The "meat/cheese/sauce" layers have the head-to-head aromatic dyad units stacked with the direction of stacking parallel to the long axis of the crystal (Figure 12c,d).

The yellow material is also structured like a molecular lasagna, but with important differences compared to the orange polymorph. In the yellow polymorph, the alkyl chains are conformationally less ordered (no longer all staggered-anti) and are no longer interdigitated between layers (Figure 12e,f). Similar to the orange material; however, the head-to-tail stacked aromatic dyad units of the yellow material are also stacked with the direction of stacking parallel to the long axis of the crystal.

Note that while the general features of yellow material produced in various ways are consistent, especially with respect to dyad head-to-tail packing geometries, there are some differences. Yellow crystals grown directly from solution (**Y**) exhibit a high level of short- and long-range order as indicated from single-crystal structures. However, thermally generated yellow material derived from orange crystals (**Y***) is best described as a soft-crystalline mesophase owing to some long-range disorder not seen in the directly grown yellow crystals.

Transition Moves Through the Orange Crystal as a Wavefront. We always observed the orange-to-yellow transition starting on either end or at a crystal defect, with the majority of a given orange-to-yellow transition sweeping along the long axis of the crystal (direction of stacking) as a wavefront, and different individual layers moving at slightly different rates (Movie S1, Movie S2, and Figure 2c). The wavefronts from each end meet in the interior of the solid to complete the conversion of the entire crystal. Using in situ heating transmission XRD, we could not detect any intermediate states during the transition process. In agreement with proposed polymorphic transition mechanisms,[42] we believe the transition wavefront represents an amorphous phase boundary between **O** and **Y*** that enables the conformational switching from **O** to **Y*** through this amorphous wavefront interface. Interestingly, the fastest wavefronts move at an approximately 38 ± 4° angle relative to the crystal long axis in what behaves like a highly cooperative or concerted process.

Structural Transition "Trigger". So, what triggers the structural transition from the orange to the yellow polymorph prior to the crystal melting entirely? We propose that upon heating of the orange crystal, the structural transition "trigger" involves the local melting of the interdigitated alkyl chain layer, which therefore becomes less ordered, allowing for some motion of the alkyl chain layer, analogous to the fluidity exhibited within biological membranes. This flexibility enables translational and/or rotational motion that has been seen in other alkyl chain containing polymorphic materials.[64,67−69] This alkyl chain layer fluidity that is the proposed triggering event does not disrupt the overall crystal morphology (which is apparently still held together by the stacked aromatics), but, importantly, we are assuming that this fluidity does allow the dyad molecules to move laterally within the solid to at least a limited extent.

Even with fluidity in the alkyl chain layer, how do all of the molecules reorganize from head-to-head (**O**) to head-to-tail (**Y***) as the wavefront passes through the material without disrupting the overall crystal morphology? All **6**, **7**, and **8** polymorphs have lamellar structures with consistent phase separation of alkyl and aromatic layers. A vertical "flip" of a single dyad within an **O** stack would convert the head-to-head packing into the head-to-tail packing seen in **Y***. However, this vertical "flip" of the molecules is highly improbable as the phase separation would be lost during a "flipping" transition. The lowest energy transition pathway that maintains the microscopic morphology of the crystal is thus expected to maintain this bilayer structure, with the majority of the reorganization happening within 2D aromatic layers.

The head-to-head to head-to-tail stacking reorganization can readily occur with a limited lateral motion between adjacent layers of the dyads. Note in the structure of the orange material in Figure 12d, the polarities of the adjacent head-to-head stacks of the dyads are exactly inverted with respect to each other in alternating fashion, so that if a given dyad molecule moves laterally into either adjacent stack in the solid, it will essentially be switching from the head-to-head orientation in its own stack to a head-to-tail orientation on the adjacent stack!

Both Faster and Slower Wavefronts are Seen. Slower transition wavefronts move in variable directions; however, all share the same feature that they begin at an edge or crack and propagate toward the interior of the crystal. The slowest transition wavefronts move parallel to horizontal crystal boundaries (Figure 2c) while the fastest wavefronts move at an angle. Initiation of all thermal transitions and the subsequent propagation of the slower transition wavefronts is believed to operate through a similar nucleation and growth mechanism. A crystal edge provides opportunity for dyad translational movement that does not exist in the packed crystal interior. Local melting of the alkyl chain layer allows for mobility within layers, and lateral motion allows for conformational sampling through translational movements without disrupting the crystal morphology. Conformational sampling on the crystal edges leads to nucleation of **Y*** that then templates subsequent **Y*** growth within the same layer. As multiple nucleation sites can emerge at different locations around single crystals, and nucleation sights can have small differences in orientation, the transition creates a soft, polycrystalline **Y*** and contributes to the observation that no SCSC transition was observed, despite numerous attempts.

The darker "pixelated" region that makes up the majority of **Y***in the first four images shown in Figure 2b is attributed to soft polycrystalline domains that formed from a nucleation and growth mechanism, the major transition observed next to crystal edges and cracks when dyads are not confined in all three crystallographic dimensions.

Why Do the Fastest Wavefronts Move at an Angle? Interestingly, the fastest wavefronts move at an angle, and slower moving wavefronts speed up as an angled wavefront emerges. Because these fastest wavefronts move in a single direction through the crystal at speeds 1−2 orders of magnitude faster than the slower wavefronts, the molecular rearrangements resulting in the transition along the wavefront are likely to be more or less concerted. A reasonable mechanistic hypothesis for the orange to yellow transition also needs to explain the observed 38 ± 4° of the wavefront relative to the long axis of the crystal, noting that this angle is the same as the proposed strongest intermolecular interactions between adjacent aromatic stacks in orange crystals, the proposed C−H···O hydrogen bonds (see Figure 13). We therefore propose that once one of the molecules in the C−H···O hydrogen-bonding network moves, the hydrogen bond to an adjacent molecule is disrupted, allowing for more motion of that adjacent molecule so it moves, which disrupts the hydrogen bond to its adjacent molecule, and so on right down the entire 38° line of hydrogen bonded molecules at the wavefront. This wavefront then moves down the crystal long axis, with a cooperative motion that turns the perpendicular dyad stacks parallel through a concerted "push", where successive dyads turn like individual pages when quickly flipping through a book. To the best of our knowledge, the observation of both thermally induced transition mechanisms operating in tandem and the switch from a nucleation and growth mechanism on crystal edges to a cooperative mechanism in the crystal interior during a transition has not previously been reported.

Thermodynamic Balancing Act. DSC measurements confirmed that the orange material is the more stable at room temperature (and below) presumably because of the combination of a reasonably stable head-to-head stacking geometry, along with maximum van der Waals interactions between the perfectly ordered and close-packed staggered-anti, interdigitated alkyl chains. In the yellow form, stabilized by slightly more favorable electrostatic interactions on the periphery of the aromatic units, a more stable head-to-tail stacking geometry is present, but the alkyl chains are no longer all staggered-anti, highly ordered, close-packed, or interdigitated. Importantly, modeling indicates that for geometric reasons, the dyad molecules cannot assemble in the more stable head-to-tail aromatic stacking orientation of the yellow solid and simultaneously accommodate the close-packed, staggered-anti, interdigitated alkyl chain layer seen in the orange crystal. The bottom line is that there is an energetic and structural trade-off between the two forms; more stable side chain packing but less stable aromatic stacking geometry in the orange form, yet more stable aromatic stacking geometry with less favorable alkyl chain packing in the yellow form. Affecting this balance, there is a dominating influence of entropy so that temperature becomes determinant of stability. As mentioned above, the more highly ordered orange material is more stable at lower temperature because of larger surface area of contact and therefore an overall increased van der Waals attraction between adjacent molecules. However, at higher temperature, where ΔS becomes more dominant, the yellow material is now more stable because of the more robust aromatic stacking geometry accompanied by a decrease in overall order (so an increase in intrinsic ΔS) of the alkyl chains. Serendipitously, the temperature at which the yellow form becomes more stable than the orange form occurs for our dyad derivatives before the melting temperature of either the orange or the yellow material is reached.

Significantly, once the transition wavefront has gone through the heated crystal, cooling the solid does not bring back the orange material because the alkyl chains do not have the opportunity to repack and the material stays yellow. On the other hand, adding organic solvent vapor allows the surface alkyl chains to reorder at room temperature, regenerating the orange material only at the solid surface. Once reorganized on the surface back to the orange structure, the reorganization is propagated through the entire solid in a functional, or possibly mechanistically, reverse of the process observed upon heating.

Additional Evidence for Mechanism. One expected consequence of the proposed mechanism is that each layer reorganizes more or less independently. As the alkyl bilayer becomes more fluid, associations between molecules in different layers are lost. In other words, once alkyl chains are no longer interdigitated, the proposed mechanism would predict that lateral diffusion of dyads and realignment to give head-to-tail stacking can occur at different rates in adjacent layers. Close inspection using optical analysis of extremely thin crystals undergoing the orange-to-yellow transition indicated that indeed the lower layers, closer to the heated surface, transitioned to yellow first, apparently independently from layers farther from the heated surface, that soon followed.

The proposed mechanism would predict that the number of molecules in each layer would remain the same before and after the orange to yellow transition, but the morphology of each layer might change slightly as the molecules can diffuse laterally to some extent. Such minor changes in layer morphology, while maintaining overall layer volume, was indeed seen in the high-resolution AFM images of Figure 9.

Finally, dyad **1** was synthesized before our detailed transition model was developed. Upon prolonged heating, crystals of dyad **1** remain bright orange and do not undergo a thermally induced phase transition prior to sublimation (Figure S3). In light of the proposed mechanism, this is as predicted. The methyl groups of **1** do not form a highly ordered, interdigitated alky chain bilayer (Figure S11), so there can be no triggering of a transition that would allow lateral motion of dyads in the solid state, as required in the other derivatives as the orange-to-yellow transition is triggered.

Summary of Proposed Mechanism. To summarize, the orange crystals of **6**−**8** adopt a lamellar, layered structure, alternating between a highly ordered, interdigitated alkyl chain layer and stacked aromatic dyad cores, with the stacks aligned along the long axis of the crystals. Upon heating, the transition initiates when the alkyl chain layers become disordered, allowing for some degree of lateral diffusion and conformational sampling for dyads at a crystal phase boundary, within their own layer. Moving to either adjacent stack in the same layer allows a dyad to exchange a head-to-head stacking geometry (orange form) for a head-to-tail stacking geometry (yellow form). The transition often initiates as a nucleation and growth mechanism that can transform to a cooperative transition wavefront that propagates through the interior of the crystal. The fastest moving wavefronts have an approximately

38° angle with respect to the long axis of the crystal, corresponding to a C−H···O hydrogen bond network of dyad molecules in adjacent stacks of the orange crystals. The driving force for this process appears to be that at lower temperature, the more highly ordered orange form is lower in energy due to maximized van der Waals contacts, while at higher temperature, the less-ordered yellow form is lower in energy dictated in part by the increased importance of entropy at higher temperature. Once formed, the yellow form becomes kinetically trapped and will persist in the absence of solvent vapor. Remarkably, the orange-to-yellow transition is apparently triggered at a temperature that is very close to the temperature at which the orange and yellow forms exchange as the most stable form. Just as remarkably, the transition occurs at a temperature that is lower than the melting point of the original orange, or final yellow, solid.

■ CONCLUSION

Engineering molecular motion in the solid-state is an emerging, but under investigated, area of supramolecular chemistry. The payoff could be a new generation of smart solids, capable of a range of easily visible responses to various stimuli. We now have a clear understanding of the dynamic solid-state thermochromic behavior of our MAN-NI dyads and the complex interplay of intermolecular interactions, solid state structural architecture, and thermodynamics that come together to enable the remarkable observed orange-to-yellow color change without melting. Our MAN-NI system appears to be the first example of a polymorphic system involving a nucleation and growth mechanism that converts to a faster cooperative mechanism within the crystal interior during a transition. The MAN-NI system is also unique because it combines a dramatic visible color change with only a minimal change in microscopic crystal morphology, both of which will be important for potential practical applications. Finally, from a scientific curiosity perspective, it is also interesting to understand how such a unique head-to-head to head-to-tail stacking rearrangement could occur in a solid. We are using our newfound understanding to design next-generation stimuli-responsive solid-state systems that will incorporate tailored alkyl chain layers with optimized C−H···O hydrogen-bonding networks to modulate both transition temperatures and cooperativity in a defined way.

■ ASSOCIATED CONTENT

SI Supporting Information

The Supporting Information is available free of charge at https://pubs.acs.org/doi/10.1021/jacs.0c08137.

Experimental details and methods, Figures S1−S14, Tables S1−S12, and other information (PDF)
Crystallographic data for **1BO** (CIF)
Crystallographic data for **6O** (CIF)
Crystallographic data for **7O** (CIF)
Crystallographic data for **6Y** (CIF)
Crystallographic data for **6Y′** (CIF)
Crystallographic data for **7Y** (CIF)
Crystallographic data for **7Y′** (CIF)
Crystallographic data for **8Y** (CIF)
Movie S1: Heating of **7O** to **7Y*** (MOV)
Movie S2: Heating of **6O** to **6Y*** (MOV)
Movie S3: Change in X-ray scattering as a single crystal of **7O** is heated to **7Y*** (MOV)

■ AUTHOR INFORMATION

Corresponding Author

Brent L. Iverson − *Department of Chemistry, The University of Texas at Austin, Austin, Texas 78712, United States;* orcid.org/0000-0001-7974-3605; Email: iversonb@austin.utexas.edu

Authors

Christopher D. Wight − *Department of Chemistry, The University of Texas at Austin, Austin, Texas 78712, United States;* orcid.org/0000-0003-3389-1762
Qifan Xiao − *Department of Chemistry, The University of Texas at Austin, Austin, Texas 78712, United States;* orcid.org/0000-0001-9867-553X
Holden R. Wagner − *Department of Chemistry, The University of Texas at Austin, Austin, Texas 78712, United States;* orcid.org/0000-0001-8718-6474
Eduardo A. Hernandez − *Department of Chemistry, The University of Texas at Austin, Austin, Texas 78712, United States;* orcid.org/0000-0002-6780-2302
Vincent M. Lynch − *Department of Chemistry, The University of Texas at Austin, Austin, Texas 78712, United States;* orcid.org/0000-0002-5260-9913

Complete contact information is available at: https://pubs.acs.org/10.1021/jacs.0c08137

Author Contributions

The manuscript was written through contributions of all authors. All authors have given approval to the final version of the manuscript.

Funding

Welch Foundation Grant F-1188.

Notes

The authors declare no competing financial interest.

■ ACKNOWLEDGMENTS

We would like to thank Mr. Jon Bender for spectroscopic insight and help calculating aromatic slip-stacking displacement, Ms. Emily Raulerson for helpful conversations, and Mr. Daniel Mangel for help with excited-state TD-DFT calculations. Additional special thanks to staff at the Texas Materials Institute (TMI), especially Drs. Raluca Gearba, Steve Swinnea, and Andrei Dolocan as well as acknowledge access to the SAXSLAB Ganesha, supported by NSF MRI Grant CBET-1624659. C.D.W. would like to say a very special thanks to Dr. Richard Piner for his expertise and help with AFM imaging. We would like to further thank the UT NMR facility for the Bruker AVIII HD 500 (NIH Grant 1 S10 OD021508-01) and the UT Mass Spec facility for their valuable help. A special thanks to Prof. Nathaniel Lynd for use of his group's POM and DSC, as well as the incredibly valuable technical help from Ms. Caitlin L. Bentley and Mr. Aaron A. Burkey, as well as Prof. Sean T. Roberts for his useful advice as well as the use of his Shimadzu UV−vis spectrometer.

■ ABBREVIATIONS

DAN, 1,5-dialkoxylnaphthalene; NDI, 1,4,5,8-naphthalenetetracarboxylic diimide; NI, naphthalene monoimide; MAN, monoalkoxynaphthalene; LUMO, lowest unoccupied molecular orbital; HOMO, highest occupied molecular orbital; CT, charge-transfer; XRD, X-ray diffraction; AFM, atomic force microscopy; POM, polarized optical microscopy; DSC, differential scanning calorimetry; PhMe, toluene; EtOAc, ethyl acetate; DCM, dichloromethane; MeCN, acetonitrile; THF, tetrahydrofuran; GIWAXS, grazing-incidence wide-angle X-ray scattering; BFDH, Bravais, Friedel, Donnay, and Harker

■ REFERENCES

(1) Salonen, L. M.; Ellermann, M.; Diederich, F. Aromatic Rings in Chemical and Biological Recognition: Energetics and Structures. *Angew. Chem., Int. Ed.* **2011**, *50* (21), 4808−4842.

(2) Chen, T.; Li, M.; Liu, J. $\pi-\pi$ Stacking Interaction: A Nondestructive and Facile Means in Material Engineering for Bioapplications. *Cryst. Growth Des.* **2018**, *18* (5), 2765−2783.

(3) Thakuria, R.; Nath, N. K.; Saha, B. K. The Nature and Applications of $\pi-\pi$ Interactions: A Perspective. *Cryst. Growth Des.* **2019**, *19* (2), 523−528.

(4) Neel, A. J.; Hilton, M. J.; Sigman, M. S.; Toste, F. D. Exploiting non-covalent π interactions for catalyst design. *Nature* **2017**, *543* (7647), 637−646.

(5) Jung, H.; Schrader, M.; Kim, D.; Baik, M.-H.; Park, Y.; Chang, S. Harnessing Secondary Coordination Sphere Interactions That Enable the Selective Amidation of Benzylic C−H Bonds. *J. Am. Chem. Soc.* **2019**, *141* (38), 15356−15366.

(6) Yuan, C.; Ji, W.; Xing, R.; Li, J.; Gazit, E.; Yan, X. Hierarchically oriented organization in supramolecular peptide crystals. *Nature Reviews Chemistry* **2019**, 3 (10), 567−588.

(7) Huo, G.-F.; Shi, X.; Tu, Q.; Hu, Y.-X.; Wu, G.-Y.; Yin, G.-Q.; Li, X.; Xu, L.; Ding, H.-M.; Yang, H.-B. Radical-Induced Hierarchical Self-Assembly Involving Supramolecular Coordination Complexes in Both Solution and Solid States. *J. Am. Chem. Soc.* **2019**, *141* (40), 16014−16023.

(8) Su, F.; Chen, G.; Korevaar, P. A.; Pan, F.; Liu, H.; Guo, Z.; Schenning, A. P. H. J.; Zhang, H.-J.; Lin, J.; Jiang, Y.-B. Discrete π-Stacks from Self-Assembled Perylenediimide Analogues. *Angew. Chem., Int. Ed.* **2019**, *58* (43), 15273−15277.

(9) Cozzi, F.; Cinquini, M.; Annuziata, R.; Siegel, J. S. Dominance of polar/.pi. over charge-transfer effects in stacked phenyl interactions. *J. Am. Chem. Soc.* **1993**, *115* (12), 5330−5331.

(10) Hunter, C. A.; Sanders, J. K. M. The nature of. pi.-. pi. interactions. *J. Am. Chem. Soc.* **1990**, *112* (14), 5525−5534.

(11) Rashkin, M. J.; Waters, M. L. Unexpected Substituent Effects in Offset π-π Stacked Interactions in Water. *J. Am. Chem. Soc.* **2002**, *124* (9), 1860−1861.

(12) Wheeler, S. E.; Houk, K. N. Substituent Effects in the Benzene Dimer are Due to Direct Interactions of the Substituents with the Unsubstituted Benzene. *J. Am. Chem. Soc.* **2008**, *130* (33), 10854−10855.

(13) Wheeler, S. E.; Houk, K. N. Substituent Effects in Cation/π Interactions and Electrostatic Potentials above the Centers of Substituted Benzenes Are Due Primarily to Through-Space Effects of the Substituents. *J. Am. Chem. Soc.* **2009**, *131* (9), 3126−3127.

(14) Wheeler, S. E. Local Nature of Substituent Effects in Stacking Interactions. *J. Am. Chem. Soc.* **2011**, *133* (26), 10262−10274.

(15) Bloom, J. W. G.; Wheeler, S. E. Taking the Aromaticity out of Aromatic Interactions. *Angew. Chem., Int. Ed.* **2011**, *50* (34), 7847−7849.

(16) Wheeler, S. E. Understanding Substituent Effects in Non-covalent Interactions Involving Aromatic Rings. *Acc. Chem. Res.* **2013**, *46* (4), 1029−1038.

(17) Wheeler, S. E.; Bloom, J. W. G. Toward a More Complete Understanding of Noncovalent Interactions Involving Aromatic Rings. *J. Phys. Chem. A* **2014**, *118* (32), 6133−6147.

(18) Carroll, W. R.; Pellechia, P.; Shimizu, K. D. A Rigid Molecular Balance for Measuring Face-to-Face Arene-Arene Interactions. *Org. Lett.* **2008**, *10* (16), 3547−3550.

(19) Hwang, J.; Li, P.; Carroll, W. R.; Smith, M. D.; Pellechia, P. J.; Shimizu, K. D. Additivity of Substituent Effects in Aromatic Stacking Interactions. *J. Am. Chem. Soc.* **2014**, *136* (40), 14060−14067.

(20) Hwang, J. W.; Li, P.; Shimizu, K. D. Synergy between experimental and computational studies of aromatic stacking interactions. *Org. Biomol. Chem.* **2017**, *15* (7), 1554−1564.

(21) Lokey, R. S.; Iverson, B. L. Synthetic molecules that fold into a pleated secondary structure in solution. *Nature* **1995**, *375* (6529), 303.

(22) Nguyen, J. Q.; Iverson, B. L. An Amphiphilic Folding Molecule That Undergoes an Irreversible Conformational Change. *J. Am. Chem. Soc.* **1999**, *121* (11), 2639−2640.

(23) Zych, A. J.; Iverson, B. L. Synthesis and Conformational Characterization of Tethered, Self-Complexing 1,5-Dialkoxynaphthalene/1,4,5,8-Naphthalenetetracarboxylic Diimide Systems. *J. Am. Chem. Soc.* **2000**, *122* (37), 8898−8909.

(24) Cubberley, M. S.; Iverson, B. L. 1H NMR Investigation of Solvent Effects in Aromatic Stacking Interactions. *J. Am. Chem. Soc.* **2001**, *123* (31), 7560−7563.

(25) Gabriel, G. J.; Iverson, B. L. Aromatic Oligomers that Form Hetero Duplexes in Aqueous Solution. *J. Am. Chem. Soc.* **2002**, *124* (51), 15174−15175.

(26) Zych, A. J.; Iverson, B. L. Conformational Modularity of an Abiotic Secondary-Structure Motif in Aqueous Solution. *Helv. Chim. Acta* **2002**, *85* (10), 3294−3300.

(27) Gabriel, G. J.; Sorey, S.; Iverson, B. L. Altering the Folding Patterns of Naphthyl Trimers. *J. Am. Chem. Soc.* **2005**, *127* (8), 2637−2640.

(28) Bradford, V. J.; Iverson, B. L. Amyloid-like Behavior in Abiotic, Amphiphilic Foldamers. *J. Am. Chem. Soc.* **2008**, *130* (4), 1517−1524.

(29) Peebles, C.; Piland, R.; Iverson, B. L. More than Meets the Eye: Conformational Switching of a Stacked Dialkoxynaphthalene−Naphthalenetetracarboxylic diimide (DAN−NDI) Foldamer to an NDI−NDI Fibril Aggregate. *Chem. - Eur. J.* **2013**, *19* (35), 11598−11602.

(30) Reczek, J. J.; Villazor, K. R.; Lynch, V.; Swager, T. M.; Iverson, B. L. Tunable Columnar Mesophases Utilizing C2 Symmetric Aromatic Donor-Acceptor Complexes. *J. Am. Chem. Soc.* **2006**, *128* (24), 7995−8002.

(31) Reczek, J. J.; Iverson, B. L. Using Aromatic Donor Acceptor Interactions to Affect Macromolecular Assembly. *Macromolecules* **2006**, *39* (17), 5601−5603.

(32) Alvey, P. M.; Reczek, J. J.; Lynch, V.; Iverson, B. L. A Systematic Study of Thermochromic Aromatic Donor-Acceptor Materials. *J. Org. Chem.* **2010**, *75* (22), 7682−7690.

(33) Peebles, C.; Alvey, P. M.; Lynch, V.; Iverson, B. L. Time-Dependent Solid-State Polymorphism of a Series of Donor−Acceptor Dyads. *Cryst. Growth Des.* **2014**, *14* (1), 290−299.

(34) Peebles, C.; Wight, C. D.; Iverson, B. L. Solution- and solid-state photophysical and stimuli-responsive behavior in conjugated monoalkoxynaphthalene-naphthalimide donor-acceptor dyads. *J. Mater. Chem. C* **2015**, 3 (46), 12156−12163.

(35) Shao, H.; Nguyen, T.; Romano, N. C.; Modarelli, D. A.; Parquette, J. R. Self-Assembly of 1-D n-Type Nanostructures Based on Naphthalene Diimide-Appended Dipeptides. *J. Am. Chem. Soc.* **2009**, *131* (45), 16374−16376.

(36) Shao, H.; Parquette, J. R. A [small pi]-conjugated hydrogel based on an Fmoc-dipeptide naphthalene diimide semiconductor. *Chem. Commun.* **2010**, *46* (24), 4285−4287.

(37) Spano, F. C. The spectral signatures of Frenkel polarons in H- and J-aggregates.(Report). *Acc. Chem. Res.* **2010**, *43* (3), 429−439.

(38) Varghese, S.; Das, S. Role of Molecular Packing in Determining Solid-State Optical Properties of π-Conjugated Materials. *J. Phys. Chem. Lett.* **2011**, 2 (8), 863−873.

(39) Hestand, N. J.; Spano, F. C. Molecular Aggregate Photophysics beyond the Kasha Model: Novel Design Principles for Organic Materials. *Acc. Chem. Res.* **2017**, *50* (2), 341−350.

(40) Gentili, D.; Gazzano, M.; Melucci, M.; Jones, D.; Cavallini, M. Polymorphism as an additional functionality of materials for technological applications at surfaces and interfaces. *Chem. Soc. Rev.* **2019**, *48* (9), 2502−2517.

(41) Seki, T.; Ito, H. Molecular-Level Understanding of Structural Changes of Organic Crystals Induced by Macroscopic Mechanical Stimulation. *Chem. - Eur. J.* **2016**, *22* (13), 4322−4329.

(42) Anwar, J.; Zahn, D. Polymorphic phase transitions: Macroscopic theory and molecular simulation. *Adv. Drug Delivery Rev.* **2017**, *117*, 47−70.

(43) Herbstein, F. On the mechanism of some first-order enantiotropic solid-state phase transitions: from Simon through Ubbelohde to Mnyukh. *Acta Crystallogr., Sect. B: Struct. Sci.* **2006**, *62* (3), 341−383.

(44) Zhao, W.; He, Z.; Peng, Q.; Lam, J. W. Y.; Ma, H.; Qiu, Z.; Chen, Y.; Zhao, Z.; Shuai, Z.; Dong, Y.; Tang, B. Z. Highly sensitive switching of solid-state luminescence by controlling intersystem crossing. *Nat. Commun.* **2018**, *9* (1), 3044.

(45) Yagai, S.; Seki, T.; Aonuma, H.; Kawaguchi, K.; Karatsu, T.; Okura, T.; Sakon, A.; Uekusa, H.; Ito, H. Mechanochromic Luminescence Based on Crystal-to-Crystal Transformation Mediated by a Transient Amorphous State. *Chem. Mater.* **2016**, *28* (1), 234−241.

(46) Yagai, S.; Okamura, S.; Nakano, Y.; Yamauchi, M.; Kishikawa, K.; Karatsu, T.; Kitamura, A.; Ueno, A.; Kuzuhara, D.; Yamada, H.; Seki, T.; Ito, H. Design amphiphilic dipolar *π*-systems for stimuli-responsive luminescent materials using metastable states. *Nat. Commun.* **2014**, *5*, 4013.

(47) Li, P.; Maier, J. M.; Hwang, J.; Smith, M. D.; Krause, J. A.; Mullis, B. T.; Strickland, S. M. S.; Shimizu, K. D. Solvent-induced reversible solid-state colour change of an intramolecular charge-transfer complex. *Chem. Commun.* **2015**, *51* (79), 14809−14812.

(48) Dharmarwardana, M.; Arimilli, B. S.; Luzuriaga, M. A.; Kwon, S.; Lee, H.; Appuhamillage, G. A.; McCandless, G. T.; Smaldone, R. A.; Gassensmith, J. J. The thermo-responsive behavior in molecular crystals of naphthalene diimides and their 3D printed thermochromic composites. *CrystEngComm* **2018**, *20* (39), 6054−6060.

(49) Yuan, T.; Vazquez, M.; Goldner, A. N.; Xu, Y.; Contrucci, R.; Firestone, M. A.; Olson, M. A.; Fang, L. Versatile Thermochromic Supramolecular Materials Based on Competing Charge Transfer Interactions. *Adv. Funct. Mater.* **2016**, *26* (47), 8604−8612.

(50) Yuan, T.; Xu, Y.; Zhu, C.; Jiang, Z.; Sue, H.-J.; Fang, L.; Olson, M. A. Tunable Thermochromism of Multifunctional Charge-Transfer-Based Supramolecular Materials Assembled in Water. *Chem. Mater.* **2017**, *29* (23), 9937−9945.

(51) Xu, Y.; Yuan, T.; Nour, H. F.; Fang, L.; Olson, M. A. Bis-Bipyridinium Gemini Surfactant-Based Supramolecular Helical Fibers and Solid State Thermochromism. *Chem. - Eur. J.* **2018**, *24* (62), 16558−16569.

(52) Le, A. K.; Bender, J. A.; Arias, D. H.; Cotton, D. E.; Johnson, J. C.; Roberts, S. T. Singlet Fission Involves an Interplay between Energetic Driving Force and Electronic Coupling in Perylenediimide Films. *J. Am. Chem. Soc.* **2018**, *140* (2), 814−826.

(53) Xue, S.; Qiu, X.; Sun, Q.; Yang, W. Alkyl length effects on solid-state fluorescence and mechanochromic behavior of small organic luminophores. *J. Mater. Chem. C* **2016**, *4* (8), 1568−1578.

(54) Jin, M.; Seki, T.; Ito, H. Mechano-Responsive Luminescence via Crystal-to-Crystal Phase Transitions between Chiral and Non-Chiral Space Groups. *J. Am. Chem. Soc.* **2017**, *139* (22), 7452−7455.

(55) Jin, M.; Sumitani, T.; Sato, H.; Seki, T.; Ito, H. Mechanical-Stimulation-Triggered and Solvent-Vapor-Induced Reverse Single-Crystal-to-Single-Crystal Phase Transitions with Alterations of the Luminescence Color. *J. Am. Chem. Soc.* **2018**, *140* (8), 2875−2879.

(56) Cruz-Cabeza, A. J.; Reutzel-Edens, S. M.; Bernstein, J. Facts and fictions about polymorphism. *Chem. Soc. Rev.* **2015**, *44* (23), 8619−8635.

(57) Anwar, J.; Tuble, S. C.; Kendrick, J. Concerted Molecular Displacements in a Thermally-Induced Solid-State Transformation in Crystals of DL-Norleucine. *J. Am. Chem. Soc.* **2007**, *129* (9), 2542−2547.

(58) Beckham, G. T.; Peters, B.; Starbuck, C.; Variankaval, N.; Trout, B. L. Surface-Mediated Nucleation in the Solid-State Polymorph Transformation of Terephthalic Acid. *J. Am. Chem. Soc.* **2007**, *129* (15), 4714−4723.

(59) Yao, Z.-S.; Guan, H.; Shiota, Y.; He, C.-T.; Wang, X.-L.; Wu, S.-Q.; Zheng, X.; Su, S.-Q.; Yoshizawa, K.; Kong, X.; Sato, O.; Tao, J. Giant anisotropic thermal expansion actuated by thermodynamically assisted reorientation of imidazoliums in a single crystal. *Nat. Commun.* **2019**, *10* (1), 4805.

(60) Duan, Y.; Semin, S.; Tinnemans, P.; Cuppen, H.; Xu, J.; Rasing, T. Robust thermoelastic microactuator based on an organic molecular crystal. *Nat. Commun.* **2019**, *10* (1), 4573.

(61) Das, D.; Jacobs, T.; Barbour, L. J. Exceptionally large positive and negative anisotropic thermal expansion of an organic crystalline material. *Nat. Mater.* **2010**, *9* (1), 36−39.

(62) Takamizawa, S.; Miyamoto, Y. Superelastic Organic Crystals. *Angew. Chem., Int. Ed.* **2014**, *53* (27), 6970−6973.

(63) Yao, Z.-S.; Mito, M.; Kamachi, T.; Shiota, Y.; Yoshizawa, K.; Azuma, N.; Miyazaki, Y.; Takahashi, K.; Zhang, K.; Nakanishi, T.; Kang, S.; Kanegawa, S.; Sato, O. Molecular motor-driven abrupt anisotropic shape change in a single crystal of a Ni complex. *Nat. Chem.* **2014**, *6* (12), 1079−1083.

(64) Su, S.-Q.; Kamachi, T.; Yao, Z.-S.; Huang, Y.-G.; Shiota, Y.; Yoshizawa, K.; Azuma, N.; Miyazaki, Y.; Nakano, M.; Maruta, G.; Takeda, S.; Kang, S.; Kanegawa, S.; Sato, O. Assembling an alkyl rotor to access abrupt and reversible crystalline deformation of a cobalt(II) complex. *Nat. Commun.* **2015**, *6* (1), 8810.

(65) Thirumalai, R.; Mukhopadhyay, R. D.; Praveen, V. K.; Ajayaghosh, A. A slippery molecular assembly allows water as a self-erasable security marker. *Sci. Rep.* **2015**, *5* (1), 9842.

(66) Karothu, D. P.; Weston, J.; Desta, I. T.; Naumov, P. Shape-Memory and Self-Healing Effects in Mechanosalient Molecular Crystals. *J. Am. Chem. Soc.* **2016**, *138* (40), 13298−13306.

(67) Abe, Y.; Savikhin, V.; Yin, J.; Grimsdale, A. C.; Soci, C.; Toney, M. F.; Lam, Y. M. Unique Reversible Crystal-to-Crystal Phase Transition—Structural and Functional Properties of Fused Ladder Thienoarenes. *Chem. Mater.* **2017**, *29* (18), 7686−7696.

(68) Chung, H.; Dudenko, D.; Zhang, F.; D'Avino, G.; Ruzié, C.; Richard, A.; Schweicher, G.; Cornil, J.; Beljonne, D.; Geerts, Y.; Diao, Y. Rotator side chains trigger cooperative transition for shape and function memory effect in organic semiconductors. *Nat. Commun.* **2018**, *9* (1), 278.

(69) Chung, H.; Chen, S.; Sengar, N.; Davies, D. W.; Garbay, G.; Geerts, Y. H.; Clancy, P.; Diao, Y. Single Atom Substitution Alters the Polymorphic Transition Mechanism in Organic Electronic Crystals. *Chem. Mater.* **2019**, *31* (21), 9115−9126.

(70) Seki, T.; Mashimo, T.; Ito, H. Anisotropic strain release in a thermosalient crystal: correlation between the microscopic orientation of molecular rearrangements and the macroscopic mechanical motion. *Chemical Science* **2019**, *10* (15), 4185−4191.

(71) DeLongchamp, D. M.; Kline, R. J.; Fischer, D. A.; Richter, L. J.; Toney, M. F. Molecular Characterization of Organic Electronic Films. *Adv. Mater.* **2011**, *23* (3), 319−337.

(72) Jiang, Z. GIXSGUI: a MATLAB toolbox for grazing-incidence X-ray scattering data visualization and reduction, and indexing of buried three-dimensional periodic nanostructured films. *J. Appl. Crystallogr.* **2015**, *48* (3), 917−926.